



Cite this: DOI: 10.1039/d1en00225b

Boosting the photocatalytic degradation of ethyl acetate by a Z-scheme Au-TiO₂@NH₂-UiO-66 heterojunction with ultrafine Au as an electron mediator†

Hongli Liu,^{ab} Xiaoyi Chang,^{ab} Xiaoxun Liu,^{ab} Guiying Li,^{ab} Weiping Zhang^{ab} and Taicheng An^{id}*^{ab}

TiO₂ based photocatalytic oxidation has been regarded as a promising technology for VOC removal, although it remains challenging in view of the limited visible light response and low photogenerated charge separation efficiency. Herein, a charge space separated Z-scheme Au-TiO₂@NH₂-UiO-66 photocatalyst was synthesized for highly efficient degradation of VOCs by encapsulation of Au and TiO₂ into visible light responsive NH₂-UiO-66 with Au nanoclusters as electron mediators. The obtained Au-TiO₂@NH₂-UiO-66 nanocomposite could broaden the light absorption of TiO₂ from the UV to visible region due to the excellent localized surface plasmon resonance of Au nanoclusters confirmed by UV-vis diffuse reflectance. Furthermore, electron paramagnetic resonance, photoelectrochemical measurements, steady-state PL spectra and time-resolved PL spectra unveil that the Au-TiO₂@NH₂-UiO-66 ternary photocatalyst followed the Z-scheme mechanism and the ultrafine Au on this heterojunction as an electron mediator can significantly accelerate photogenerated electron transfer. Due to the enhanced interfacial electron transfer by the Au electron mediator and high redox abilities of photogenerated carriers in the Z-scheme heterojunction, the Au-TiO₂@NH₂-UiO-66 nanocomposite greatly boosted the separation efficiency of photogenerated electron-hole pairs, thus producing abundant strong oxidative species, including photogenerated holes, [•]O²⁻ and [•]OH radicals, to mineralize VOCs. Impressively, the mineralization efficiency reached 85% at 94.6% ethyl acetate degradation over the 1 wt% Au-TiO₂@NH₂-UiO-66 photocatalyst within 360 min of xenon lamp irradiation, which was 12.1, 10.6 and 2.83 times higher than that of TiO₂, NH₂-UiO-66 and TiO₂@NH₂-UiO-66, respectively. This work would provide a valuable guideline in the synthesis of highly efficient visible light responsive photocatalysts for VOC degradation.

Received 10th March 2021,
Accepted 4th July 2021

DOI: 10.1039/d1en00225b

rsc.li/es-nano

Environmental significance

Exploitation of highly efficient TiO₂ based catalysts for photocatalytic degradation of VOCs under visible light irradiation is highly desirable yet challenging. Herein, a charge space separated Z-scheme Au-TiO₂@NH₂-UiO-66 photocatalyst was synthesized by encapsulation of tiny TiO₂ into visible light responsive NH₂-UiO-66 with Au nanoclusters as their connecting bridge. The obtained Au-TiO₂@NH₂-UiO-66 not only broadened the light absorption of TiO₂ from the UV to visible region, but also promoted the photogenerated charge transfer and separation. Importantly, the mineralization ratio of ethyl acetate reached 85% over Au-TiO₂@NH₂-UiO-66 under visible light irradiation, which was 12.1 times higher than that of TiO₂. This work will provide an advantageous blueprint to construct highly efficient photocatalysts *via* the combination of visible light responsive MOFs and other semiconductors for VOC degradation.

^a Guangdong Key Laboratory of Environmental Catalysis and Health Risk Control, Guangdong-Hong Kong-Macao Joint Laboratory for Contaminants Exposure and Health, Institute of Environmental Health and Pollution control, Guangdong University of Technology, Guangzhou 510006, China. E-mail: antic99@gdut.edu.cn

^b Guangdong Engineering Technology Research Center for Photocatalytic Technology Integration and Equipment, Guangzhou Key Laboratory of Environmental Catalysis and Pollution Control, School of Environmental Science and Engineering, Guangdong University of Technology, Guangzhou 510006, China
† Electronic supplementary information (ESI) available: N₂ adsorption-desorption isotherms, adsorption kinetic curves, XPS spectra as well as Mott Schottky plots. See DOI: 10.1039/d1en00225b

1. Introduction

Volatile organic compounds (VOCs) as typical air pollutants have brought a lot of hazards to human health and the ecological environment even at very low concentrations, such as teratogenesis, mutagenesis, cancer, tropospheric ozone depletion and photochemical smog.¹⁻³ Consequently, the development of effective VOC removal technologies with minimal environmental impact has increasingly attracted

considerable attention, and various techniques have been successfully explored including adsorption, sorption, photocatalytic oxidation, catalytic oxidation, biological treatment, *etc.*^{3–18} Among these technologies, semiconductor photocatalytic oxidation has been regarded as an intriguing option for VOC removal because it has the potential to mineralize various VOCs into eco-friendly H₂O and CO₂ as final products without extra energy input.^{8–18} In this respect, TiO₂ has high stability, low price, and a sufficiently positive valence band (*ca.* 2.9 V) to satisfy the mineralization of VOCs, and thus has been one of the most widely investigated and promising photocatalysts.^{14–18} Unfortunately, it often suffers from poor photocatalytic efficiency under visible or solar light irradiation because of its narrow light response range and easy recombination of photogenerated electron–hole pairs,^{14–18} critically hampering its potential applications in photocatalytic degradation of VOCs.

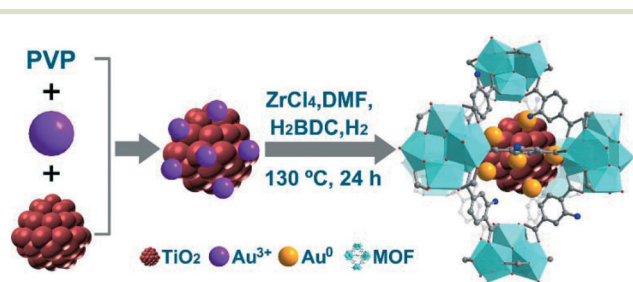
Constructing a Z-scheme heterojunction has proven to be an effective strategy to improve the photocatalytic performance of photocatalysts,^{19–25} which is generally composed of two separate semiconductors (PS I and PS II). In the Z-scheme system, the photogenerated electrons with a less negative position on the conduction band of PS I will recombine with the photogenerated holes with a less positive position on the valence band of PS II, while the photogenerated electrons on the conduction band of PS II and the photogenerated holes on the valence band of PS I will remain. As a result, the efficiency of photogenerated electron–hole separation in this heterostructure would be promoted. More importantly, the remaining photogenerated electrons and holes in the Z-scheme photocatalytic system could guarantee a stronger redox ability compared with its corresponding isolated semiconductors. Therefore, coupling TiO₂ with other suitable semiconductors to construct Z-scheme heterojunction photocatalysts would be a feasible strategy to boost the photocatalytic degradation performance for VOCs.

Porous semiconductors have received a great deal of research interest because their large surface area and high pore volumes could offer facile transport and diffusion of substrates and allow for exposure of accessible active sites as much as possible.^{26–28} Moreover, their porous structures could afford shorter charge carrier transfer distances to reach the surface of the catalyst and the substrates compared to their bulk counterparts, leading to efficient separation of photogenerated electron–hole pairs. As a particular class of porous materials, metal–organic frameworks (MOFs) with many fascinating characteristics^{29–31} might offer new opportunities to construct highly efficient Z-scheme heterojunction photocatalysts for VOC degradation by rational integration of TiO₂ with MOFs. Apart from the common virtues of porous materials, the enormous interconnected 3D open cavities in MOFs enable light to easily penetrate and largely alleviate the light shielding phenomenon. More importantly, the metal cluster nodes in MOFs isolated by the organic linkers and the pores of the MOFs can behave as

semiconductor dots, thus making MOFs (such as NH₂-UiO-66, UiO-66, Fe-MIL-101, Fe-MIL-100 and NH₂-MIL-125) exhibit semiconductor-like behaviors.^{32–36} Furthermore, there have been a few reports on the construction of Z-scheme photocatalysts *via* the integration of conventional semiconductors with MOFs for dye photodegradation, CO₂ reduction, and photocatalytic H₂ evolution.^{37–42} However, due to the limited light response in the visible region and poor electron conductivity of most MOFs, it is still difficult to obtain satisfactory photocatalytic efficiency.

On the other hand, it has been demonstrated that some plasmon-inducing metals can serve as excellent electron mediators to promote the transfer of charge carriers when they are deposited on the surface of semiconductor heterostructures.^{20,24,42–44} In particular, nanostructured Au can absorb light in the visible to near infrared region due to its localized surface plasmon resonance (LSPR).⁴⁵ To maximize the separation efficiency of electron–hole pairs and the visible-light utilization, the construction of a Au-TiO₂@MOF ternary Z-scheme photocatalyst with Au as an electron mediator was proposed by integrating tiny TiO₂ nanoparticle supported Au into a visible light responsive MOF. The advantage of this design would maximize the exposure of TiO₂ and Au, and allow the three components to be in good contact with each other within the photocatalyst by improving the interfacial contact area. The intimate contacts at each interface and the plasmonic Au with excellent LSPR would enable the smooth migration of photogenerated charge, thus being expected to accelerate the electron–hole separation and subsequently boosting the degradation efficiencies of VOCs.

Herein, as a proof-of-concept, tiny TiO₂ nanoparticle supported Au clusters were incorporated into NH₂-UiO-66 to construct a Z-scheme photocatalyst for promoting the photocatalytic degradation of VOCs (Scheme 1). NH₂-UiO-66 was selected due to its great stability, large surface area, appropriate band structure that matched with TiO₂, and visible-light responsive nature. To strengthen the interface contact, Au³⁺ was firstly supported on TiO₂ with the assistance of polyvinyl pyrrolidone (PVP). Subsequently, the resultant Au³⁺/TiO₂ served as the core for the growth of the outer NH₂-UiO-66 shell while Au³⁺ was *in situ* reduced to Au⁰ clusters by H₂ and DMF during the growth process of NH₂-



Scheme 1 Illustration of the preparation of the Au-TiO₂@NH₂-UiO-66 nanocomposite.

UiO-66. The as-synthesized Au-TiO₂@NH₂-UiO-66 heterojunction exhibited remarkably enhanced removal capacity and mineralization efficiency in the visible light driven photocatalytic oxidation of VOCs. Finally, a possible mechanism for the photocatalytic oxidation of typical VOCs over Au-TiO₂@NH₂-UiO-66 was also tentatively proposed.

2. Experimental section

2.1 Material synthesis

All chemical reagents were obtained from commercial sources and used without further purification.

Synthesis of NH₂-UiO-66. NH₂-UiO-66 was synthesized following a previous report with slight modifications.⁴⁶ Typically, 0.1 mol of ZrCl₄, 0.1 mol of 2-aminoterephthalic acid, 1.7 mL of H₂O, and 8 mL of acetic acid were added into 80 mL of DMF in a 250 mL Schlenk tube. Then, the above mixture was treated by ultra-sonication for 30 min and was heated further at 130 °C for 24 h. Subsequently, the resultant faint yellow solid was isolated, washed with DMF and methanol, and finally activated at 150 °C for 12 h under vacuum.

Synthesis of Au-TiO₂, Au/NH₂-UiO-66 and TiO₂@NH₂-UiO-66 composites. TiO₂ nanoparticles were synthesized according to procedures reported in the literature.⁴⁷ As for the synthesis of TiO₂@NH₂-UiO-66, 30 mg of TiO₂ was initially dispersed in 50 mL of absolute alcohol by ultra-sonication for 1 h. 625 mg of PVP was added into the above mixture and further stirred for 24 h. After that, the PVP stabilized TiO₂ nanoparticles were collected, washed with DMF, and dispersed in 10 mL of DMF. Subsequently, 10 mL of TiO₂ nanoparticle solution was added into a precursor solution of NH₂-UiO-66 in a 250 mL Schlenk tube which contained 0.1 mmol of ZrCl₄, 0.1 mmol of 2-aminoterephthalic acid, 1.7 mL of H₂O, 8 mL of acetic acid and 70 mL of DMF. The tube was sealed and reacted at 130 °C for 24 h. The as-synthesized sample was isolated, washed with DMF and methanol, and finally activated at 150 °C for 12 h under vacuum.

For the synthesis of Au-TiO₂, 1.7 mL of AuCl₃ aqueous solution was added into 10 mL of PVP stabilized TiO₂ nanoparticle DMF solution and stirred for 4 h. Subsequently, the solution under a H₂ atmosphere was heated at 130 °C for 24 h. For the synthesis of Au/NH₂-UiO-66, 1.7 mL of AuCl₃ aqueous solution was added into the precursor solution of NH₂-UiO-66 under a H₂ atmosphere and further reacted at 130 °C for 24 h. Finally, the as-synthesized Au-TiO₂ and Au/NH₂-UiO-66 samples were isolated and activated using the same procedures as TiO₂@NH₂-UiO-66.

Synthesis of Au-TiO₂@NH₂-UiO-66 composites. For the Au-TiO₂@NH₂-UiO-66 composite with 1 wt% Au loading (1 wt% Au-TiO₂@NH₂-UiO-66), the preparation process was similar to that of TiO₂@NH₂-UiO-66. Typically, 1.7 mL of AuCl₃ aqueous solution was added into 10 mL of PVP stabilized TiO₂ nanoparticle DMF solution and stirred for 4 h. After that, the solution was added to the precursor

solution of NH₂-UiO-66 under a H₂ atmosphere and further reacted at 130 °C for 24 h. The as-synthesized sample was isolated, washed with DMF and methanol, and finally activated at 150 °C for 12 h under vacuum. For the Au-TiO₂@NH₂-UiO-66 composites with 0.1 and 0.5 wt% Au loading, the synthetic procedures were exactly the same as those for the 1 wt% Au-TiO₂@NH₂-UiO-66 composite, except that the volumes of AuCl₃ aqueous solution were 0.17 and 0.85 mL.

2.2 Characterization

The X-ray diffraction patterns (XRD) of the synthesized samples were measured using a Bruker D8 Advance power diffractometer with a Cu K α radiation source. Fourier transform infrared spectra (FT-IR) were collected on a Thermo Fisher iS50R using the KBr disk technique. The dispersion and morphology of the synthesized samples were observed by aberration-corrected scanning transmission electron microscopy (HAADF-STEM) on a Merlin Carl Zeiss AG instrument. UV-vis diffuse reflectance spectra were recorded on an Agilent Carry 300 spectrophotometer with BaSO₄ as a standard reference. X-ray photoelectron spectroscopy (XPS) measurements were performed on a Thermo Fisher Escalab Xi⁺ spectrometer. The surface areas and porosity of the samples were investigated on a Belsorp-Max using the N₂ adsorption-desorption method at 77 K. The contents of Au and TiO₂ in the samples were determined quantitatively by atomic absorption spectroscopy (AAS) on a HITACHI Z-2000.

Photo-electrochemical properties and Mott-Schottky plots were obtained on a Shanghai Chenhua CHI 600E station in a typical three-electrode system in 0.5 M Na₂SO₄ aqueous solution. In the three-electrode system, an Ag/AgCl electrode, platinum plate and sample coated FTO glass were utilized as the reference electrode, counter electrode and working electrode, respectively. The steady-state photoluminescence (PL) spectra were recorded on a Fluorolog-3 fluorescence spectrometer. The surface temperature changes of the samples under the illumination of a 300 W xenon lamp were monitored using a Fluke TiX640 thermal imaging infrared camera. The generated $\cdot\text{OH}$ and $\cdot\text{O}^{2-}$ radicals of the samples were trapped by 5,5'-dimethyl-1-pyrroline-N-oxide (DMPO) and then measured using an electron paramagnetic resonance (EPR) spectrometer (EMXPlus-10/12).

2.3 Photocatalytic degradation and dark adsorption experiments

The photocatalytic degradation reactions of gaseous ethyl acetate were carried out in a quartz reactor in a constant flow at ambient temperature and pressure. A 300 W xenon lamp with an irradiance intensity of 303 mW cm⁻² described in our previous report³⁶ was chosen as the light source and was assembled 10 cm above the reactor. Firstly, 100 mg of photocatalyst was filled into the reactor and then pre-treated at 150 °C for 4 h under a N₂ atmosphere to remove the

possible impurities adsorbed on the surface of the photocatalyst. After cooling to room temperature, 70 ± 1 ppmv of ethyl acetate feed gas diluted with dry air was flowed into the reactor at a flow velocity of 30 mL min^{-1} , while the xenon lamp was instantly switched on to initiate the photocatalytic degradation reactions. The compositions of the remaining ethyl acetate and evolved CO_2 in the outlet gas were analysed using an online gas chromatograph with a nickel reforming furnace.

Dark adsorption tests were also performed under the same measurement conditions as described in the photocatalytic degradation experiments, except without light irradiation. The adsorption capacity of these samples for ethyl acetate was estimated based on the breakthrough curve by using a previously reported equation.⁶

3. Results and discussion

3.1 Characterization of the samples

The crystal structures of the as-synthesized TiO_2 , $\text{NH}_2\text{-UiO-66}$, $\text{TiO}_2@\text{NH}_2\text{-UiO-66}$ and $\text{Au-TiO}_2@\text{NH}_2\text{-UiO-66}$ samples were investigated *via* powder XRD. As displayed in Fig. 1a, the pure TiO_2 presented XRD characteristic peaks at 25.4 , 37.8 , 48.0 , and 53.9° , which could be assigned to the (101), (004), (200) and (105) crystal planes of anatase phase TiO_2 according to JCPDS no. 21-1272, respectively. For the pure $\text{NH}_2\text{-UiO-66}$, the characteristic diffraction peaks matched well with the already reported XRD patterns.⁴⁶ After TiO_2 nanoparticles were embedded into $\text{NH}_2\text{-UiO-66}$, the characteristic XRD peaks of the $\text{TiO}_2@\text{NH}_2\text{-UiO-66}$ nanocomposite were consistent with the parent $\text{NH}_2\text{-UiO-66}$. Moreover, there were no apparent changes in the characteristic diffraction peaks after the introduction of both Au and TiO_2 into $\text{NH}_2\text{-UiO-66}$ compared to those of $\text{NH}_2\text{-UiO-66}$. These results indicated that the incorporation of TiO_2 or both Au and TiO_2 into $\text{NH}_2\text{-UiO-66}$ did not change its structural integrity. Nevertheless, the characteristic diffraction peaks with respect to Au and TiO_2 could not be observed for both the $\text{TiO}_2@\text{NH}_2\text{-UiO-66}$ and 1 wt% $\text{Au-TiO}_2@\text{NH}_2\text{-UiO-66}$ samples, which might be relevant to their low loading amount and/or tiny particle diameter. Furthermore, the actual loading amount of TiO_2 in the $\text{TiO}_2@\text{NH}_2\text{-UiO-66}$ and 1 wt% $\text{Au-TiO}_2@\text{NH}_2\text{-UiO-66}$ nanocomposites measured by AAS was 4.97 and 5.02 wt%,

respectively, and the measured content of Au in 1 wt% $\text{Au-TiO}_2@\text{NH}_2\text{-UiO-66}$ was 0.99 wt%.

To further obtain the structural information, FT-IR measurements were also carried out. As shown in Fig. 1b and S1,[†] a broad peak in the range of $400\text{--}700 \text{ cm}^{-1}$ correlated with the O-Ti-O stretching vibration and a weak peak at 1650 cm^{-1} attributed to the hydroxyl stretching vibrations of Ti-OH bonding were observed in the pure TiO_2 sample. As for pure $\text{NH}_2\text{-UiO-66}$, the symmetric and asymmetric stretching vibrations of the COO^- groups were significantly visualized at 1386 , 1432 and 1574 cm^{-1} , respectively. Additionally, the bands at 484 cm^{-1} and 663 cm^{-1} could be assigned to the Zr-O asymmetric stretching vibrations and O=C=O bending.⁴⁸ Compared to pure $\text{NH}_2\text{-UiO-66}$, a new peak at 796 cm^{-1} appeared in both $\text{TiO}_2@\text{NH}_2\text{-UiO-66}$ and 1 wt% $\text{Au-TiO}_2@\text{NH}_2\text{-UiO-66}$, while both peaks at 484 and 663 cm^{-1} were slightly broadened and weakened, indicating the emergence of Ti-O-Zr groups.^{12,49} Nevertheless, most of the characteristic peaks of $\text{TiO}_2@\text{NH}_2\text{-UiO-66}$ and 1 wt% $\text{Au-TiO}_2@\text{NH}_2\text{-UiO-66}$ were consistent with those of $\text{NH}_2\text{-UiO-66}$. These observations suggested that the incorporation of TiO_2 and Au into $\text{NH}_2\text{-UiO-66}$ could generate interfacial contact between TiO_2 and the MOF but still maintain the structure of $\text{NH}_2\text{-UiO-66}$.

To visually observe the size and distribution of the samples, TEM measurements were further performed. TEM images showed that pure $\text{NH}_2\text{-UiO-66}$ and TiO_2 had uniform particles with sizes mostly between $80\text{--}120 \text{ nm}$ and $2\text{--}3 \text{ nm}$ (Fig. 2a and b), respectively. High-resolution TEM images displayed that the interplanar spacing of the TiO_2 lattice was about 0.209 and 0.165 nm (Fig. 2c and S2[†]), which are assigned to the (004) and (105) planes of anatase phase TiO_2 , respectively. These were in good agreement with the XRD

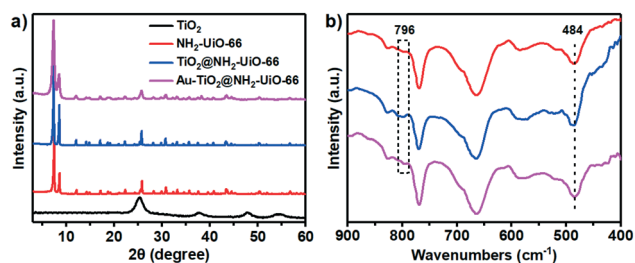


Fig. 1 Powder XRD patterns (a) and FT-IR spectra (b) of TiO_2 , pure $\text{NH}_2\text{-UiO-66}$, $\text{TiO}_2@\text{NH}_2\text{-UiO-66}$ and 1 wt% $\text{Au-TiO}_2@\text{NH}_2\text{-UiO-66}$ in the range of $400\text{--}900 \text{ cm}^{-1}$, respectively.

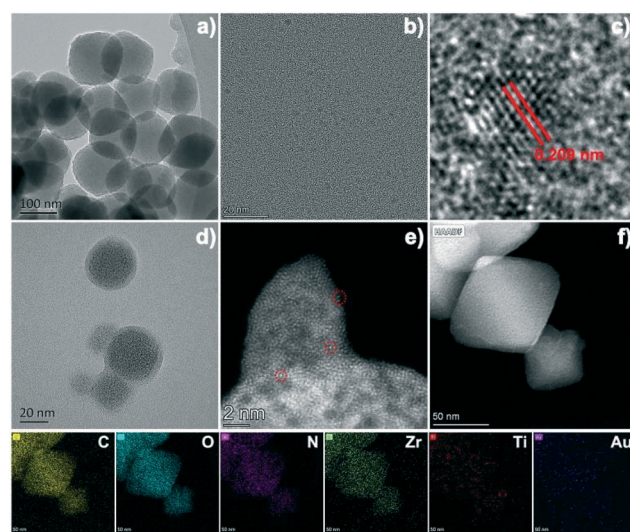


Fig. 2 TEM images of pure $\text{NH}_2\text{-UiO-66}$ (a), TiO_2 (b and c), and 1 wt% $\text{Au-TiO}_2@\text{NH}_2\text{-UiO-66}$ (d), and HAADF-STEM images (e and f) and the corresponding EDX elemental mapping of 1 wt% $\text{Au-TiO}_2@\text{NH}_2\text{-UiO-66}$, respectively.

results. As for 1 wt% Au-TiO₂@NH₂-UiO-66, TiO₂ nanoparticles were unevenly incorporated into NH₂-UiO-66 with an approximately 4 nm thick pure MOF shell (Fig. 2d), which was associated with the surfactant PVP modifying the TiO₂ surface.⁵⁰ Although the content of Au in 1 wt% Au-TiO₂@NH₂-UiO-66 was measured to be 0.99 wt% by AAS, almost no particles related to Au were observed, probably due to their small size and their location in NH₂-UiO-66 as well as the resolution limit of TEM. Gratifyingly, Au nanoclusters with ultrafine sizes were evidenced by HAADF-STEM as shown in Fig. 2e. Furthermore, the EDX mapping measurements (Fig. 2f) further demonstrated that Au and TiO₂ were homogeneously distributed throughout NH₂-UiO-66.

N₂ adsorption-desorption measurements of the as-synthesized samples at 77 K were also performed to gain their specific surface areas and porosities, and the results are summarized in Fig. S3 and Table S1.† For the TiO₂ nanoparticles, they displayed a type IV isotherm curve with a hysteresis loop, and the BET specific surface area and total pore volume were found to be 126.9 m² g⁻¹ and 0.07 cm³ g⁻¹, respectively. Comparatively, the adsorption isotherm of pure NH₂-UiO-66 exhibited sharply boosted N₂ uptake in the low pressure region and was essentially coincident with its desorption isotherm, implying that NH₂-UiO-66 possessed a microporous structure with a type I isotherm. After the introduction of TiO₂ into NH₂-UiO-66, the adsorption isotherm still maintained the typical type I isotherm of its parent NH₂-UiO-66, but the BET specific surface area and total pore volume of TiO₂@NH₂-UiO-66 decreased to 725.4 m² g⁻¹ and 0.36 cm³ g⁻¹ from 910.3 m² g⁻¹ and 0.41 cm³ g⁻¹ as compared to pure NH₂-UiO-66, respectively. These decreases could be associated with the weight contributions and the partial occupation of NH₂-UiO-66 cavities by the low porosity TiO₂ nanoparticles. When both Au and TiO₂ were incorporated into NH₂-UiO-66, the N₂ adsorption isotherm of the 1 wt% Au-TiO₂@NH₂-UiO-66 nanocomposite emerged as a mixed type I and IV curve with an apparent H3 typical hysteresis loop, which was significantly different with that of pure NH₂-UiO-66. Considering that the size of NH₂-UiO-66 was obviously reduced after the incorporation of Au and TiO₂ (Fig. 2), the resulting hysteresis loop should be associated with the aggregations of Au-TiO₂@NH₂-UiO-66 crystallites.

To acquire the optical absorption properties, the samples were further investigated by UV-vis diffuse reflectance. As observed in Fig. 3a, the TiO₂ nanoparticles only showed an absorption peak edge at *ca.* 380 nm and centered at 300 nm. As for pure NH₂-UiO-66, a strong absorption peak in the range of 300–450 nm emerged, indicating that it could harvest light from the ultraviolet region to a small part of the visible region. After introducing TiO₂ nanoparticles, it was noticed that TiO₂@NH₂-UiO-66 well inherited the optical response features of its parent NH₂-UiO-66 except for a slightly raised absorption intensity in the range of 450–800 nm. Remarkably, 1 wt% Au-TiO₂@NH₂-UiO-66 presented a new absorption peak at *ca.* 530 nm, which is derived from the typical LSPR of Au nanoparticles. Moreover, the light

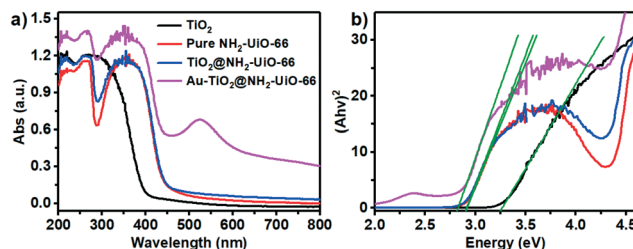


Fig. 3 UV-vis diffuse reflectance spectra (a) and the corresponding Tauc plot (b) of TiO₂, pure NH₂-UiO-66, TiO₂@NH₂-UiO-66 and 1 wt% Au-TiO₂@NH₂-UiO-66, respectively.

absorption intensities through the whole ultraviolet and visible region were boosted, especially in the visible region. These observations demonstrated that the incorporation of Au nanoparticles could effectively improve the visible light harvesting ability due to the LSPR of Au. Additionally, the band gap energy (E_g) of TiO₂, NH₂-UiO-66, TiO₂@NH₂-UiO-66 and 1 wt% Au-TiO₂@NH₂-UiO-66 was calculated to be 3.25, 2.91, 2.90 and 2.81 eV based on their corresponding ($Ah\nu$)² versus $h\nu$ curves (Fig. 3b), respectively.

3.2 Photocatalytic performance tests

Gaseous ethyl acetate, a representative oxygenated VOC, was chosen to investigate the photocatalytic activity of the as-prepared samples. As illustrated in Fig. 4a, the concentrations of ethyl acetate in the effluent gas in the presence of TiO₂, NH₂-UiO-66, TiO₂@NH₂-UiO-66 and 1 wt% Au-TiO₂@NH₂-UiO-66 dropped rapidly and then remained steady at 97.5%, 95.3%, 93.2% and 94.6% within 360 min of xenon lamp irradiation, respectively. However, the CO₂ amounts produced from ethyl acetate over the investigated samples were significantly different. As for pure TiO₂, only 23 ppmv of CO₂ was generated, meaning that approximately 7% ethyl acetate could be completely mineralized (Fig. 4b). Similarly, the pure NH₂-UiO-66 exhibited an inappreciable enhancement in the produced CO₂ amounts compared to TiO₂ and the corresponding mineralization efficiency was around 8% within 360 min of xenon lamp irradiation. These results implied that pure TiO₂ and NH₂-UiO-66 were not able to work as effective photocatalysts for the degradation of ethyl acetate under irradiation of visible light. Comparatively, after the

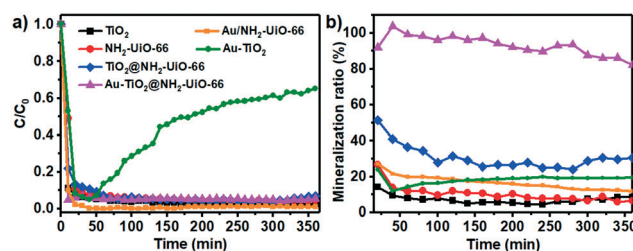


Fig. 4 Removal efficiencies (a) and mineralization efficiencies (b) of ethyl acetate during photocatalytic oxidation by TiO₂, NH₂-UiO-66, Au-TiO₂, Au/NH₂-UiO-66, TiO₂@NH₂-UiO-66 and 1 wt% Au-TiO₂@NH₂-UiO-66.

incorporation of TiO_2 into $\text{NH}_2\text{-UiO-66}$, the mineralization efficiency of ethyl acetate was drastically improved to 30% which was 3.75 and 4.29 times higher than that of pure $\text{NH}_2\text{-UiO-66}$ and TiO_2 , respectively. Furthermore, $\text{Au-TiO}_2\text{@NH}_2\text{-UiO-66}$ with different Au contents were screened and the results (Fig. S4 and S5[†]) pointed to an optimised performance of $\text{Au-TiO}_2\text{@NH}_2\text{-UiO-66}$ with 1 wt% Au loading. Noticeably, 1 wt% $\text{Au-TiO}_2\text{@NH}_2\text{-UiO-66}$ could provide a steady mineralization efficiency of around 85% for ethyl acetate during the continuous reaction for 360 min. To further verify the effect of Au on the photocatalytic activity, photocatalytic oxidation reactions with Au/TiO_2 and $\text{Au/NH}_2\text{-UiO-66}$ were also performed. Au/TiO_2 and $\text{Au/NH}_2\text{-UiO-66}$ showed 20% and 10% mineralization efficiencies within 360 min of xenon lamp irradiation, respectively, which were slightly higher than that of pure TiO_2 and $\text{NH}_2\text{-UiO-66}$ but distinctly lower than that of $\text{Au-TiO}_2\text{@NH}_2\text{-UiO-66}$. The above results indicated that excellent photocatalytic activity was not achieved by introduction of individual Au or TiO_2 into $\text{NH}_2\text{-UiO-66}$, but required the synergy among the three components. To check the stability of $\text{Au-TiO}_2\text{@NH}_2\text{-UiO-66}$ under the photocatalytic conditions, the 1 wt% $\text{Au-TiO}_2\text{@NH}_2\text{-UiO-66}$ sample after the photocatalytic reaction for 360 min was analyzed by XRD (Fig. S6[†]). The results showed that no appreciable changes in the characteristic diffraction peaks were observed after the photocatalytic reaction. The above results indicated that the $\text{Au-TiO}_2\text{@NH}_2\text{-UiO-66}$ sample was stable under the investigated photocatalytic conditions.

It has been proven that the VOC adsorption capability of a photocatalyst might have a pivotal effect on its photocatalytic activity.²⁹ Thus, dark adsorption tests were further performed in the presence of TiO_2 , $\text{NH}_2\text{-UiO-66}$, $\text{TiO}_2\text{@NH}_2\text{-UiO-66}$ and 1 wt% $\text{Au-TiO}_2\text{@NH}_2\text{-UiO-66}$ to investigate the influences of their adsorption capacities for ethyl acetate on the photocatalytic efficiencies. As shown in Fig. S7,[†] the ethyl acetate in the outlet gas rapidly disappeared within 60 min in the presence of pure TiO_2 and $\text{NH}_2\text{-UiO-66}$, and the adsorption equilibrium was reached within 780 and 3460 min, respectively. Furthermore, the equilibrium adsorption capacities of ethyl acetate on pure TiO_2 and $\text{NH}_2\text{-UiO-66}$ were calculated to be 30.97 mg g^{-1} and 621.88 mg g^{-1} based on their breakthrough curves, respectively. After the incorporation of TiO_2 into $\text{NH}_2\text{-UiO-66}$, the equilibrium adsorption capacity of ethyl acetate was slightly decreased to 146.89 mg g^{-1} compared to $\text{NH}_2\text{-UiO-66}$. Moreover, the complete breakthrough time of 1 wt% $\text{Au-TiO}_2\text{@NH}_2\text{-UiO-66}$ was extended to 2540 min and the estimated adsorption capacity was 118.29 mg g^{-1} . The above adsorption results demonstrated that $\text{Au-TiO}_2\text{@NH}_2\text{-UiO-66}$ with optimal photocatalytic activity didn't possess the highest ethyl acetate adsorption capacity, implying that the adsorption capacities of the four photocatalysts could not be responsible for their significant differences in photocatalytic activity.

Considering the excellent adsorption capacity of the investigated samples for ethyl acetate (Fig. S7[†]), the evidently different CO_2 production amounts but approximate removal efficiency would be relevant to their adsorption capacities for

ethyl acetate. That is, the instant adsorption of ethyl acetate onto the surface of TiO_2 , $\text{NH}_2\text{-UiO-66}$, $\text{TiO}_2\text{@NH}_2\text{-UiO-66}$ and $\text{Au-TiO}_2\text{@NH}_2\text{-UiO-66}$ might also occur with the photocatalytic degradation process synchronously during xenon lamp irradiation, which was also observed in our previous reports.^{10,12} Additionally, the selective conversion of ethyl acetate into CO_2 over TiO_2 , $\text{NH}_2\text{-UiO-66}$, $\text{TiO}_2\text{@NH}_2\text{-UiO-66}$ and 1 wt% $\text{Au-TiO}_2\text{@NH}_2\text{-UiO-66}$ was calculated to be 8, 9, 31 and 87%, respectively. The above results demonstrated that the rational introduction of Au and TiO_2 into $\text{NH}_2\text{-UiO-66}$ could considerably boost the photocatalytic degradation performance including the mineralization efficiency and CO_2 selectivity, which was significantly higher than that of both pure TiO_2 and $\text{NH}_2\text{-UiO-66}$ toward ethyl acetate.

3.3 Mechanism of enhanced photocatalytic efficiencies of $\text{Au-TiO}_2\text{@NH}_2\text{-UiO-66}$

We attempted to reveal the mechanism of excellent photocatalytic efficiencies of $\text{Au-TiO}_2\text{@NH}_2\text{-UiO-66}$. Initially, XPS was performed to further clarify the interfacial interaction. The XPS survey spectra (Fig. S8[†]) revealed that the 1 wt% $\text{Au-TiO}_2\text{@NH}_2\text{-UiO-66}$ nanocomposite consisted of C, O, N, Zr, Ti and Au elements. For pure $\text{NH}_2\text{-UiO-66}$, the characteristic peaks located at 182.5 eV and 184.9 eV (Fig. 5a) were ascribed to Zr 3d_{5/2} and Zr 3d_{3/2}, respectively. The three O 1s peaks at 529.8, 531.7 and 533.8 eV (Fig. 5b) were attributed to the Zr–O bond, O–H bond, and C–O bond. When TiO_2 was incorporated into $\text{NH}_2\text{-UiO-66}$, a slight positive shift of two Zr 3d_{5/2} and Zr 3d_{3/2} peaks was observed, while two Ti 2p_{3/2} and Ti 2p_{1/2} peaks showed a negative shift (Fig. 5a and c). It was noticeable that the C–O bond in the $\text{TiO}_2\text{@NH}_2\text{-UiO-66}$ sample shifted to higher binding energy by approximately 0.4 eV compared with pure $\text{NH}_2\text{-UiO-66}$.

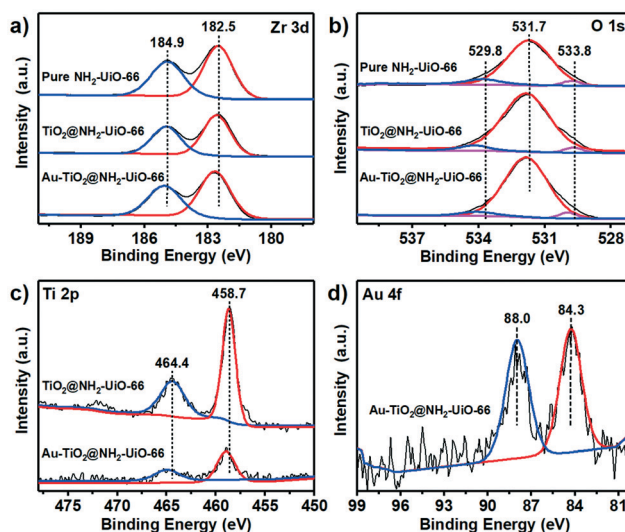


Fig. 5 XPS spectra of Zr 3d (a), O 1s (b), Ti 2p (c) and Au 4f (d) for the pure $\text{NH}_2\text{-UiO-66}$, $\text{TiO}_2\text{@NH}_2\text{-UiO-66}$ and 1 wt% $\text{Au-TiO}_2\text{@NH}_2\text{-UiO-66}$ samples, respectively.

These results demonstrated that there was strong interfacial interaction between TiO_2 and $\text{NH}_2\text{-UiO-66}$, implying the formation of a heterojunction between TiO_2 and $\text{NH}_2\text{-UiO-66}$. As displayed in Fig. 5d, the Au $4f_{5/2}$ and Au $4f_{7/2}$ peaks in 1 wt% Au- $\text{TiO}_2@NH_2\text{-UiO-66}$ were located at 88.0 eV and 84.3 eV, respectively, indicating the presence of Au (0) metal. Noticeably, compared to $\text{TiO}_2@NH_2\text{-UiO-66}$, the Zr 3d, Ti $2p_{3/2}$ and Ti $2p_{1/2}$ peaks of 1 wt% Au- $\text{TiO}_2@NH_2\text{-UiO-66}$ were all shifted to higher binding energy by approximately 0.1 eV, 0.6 eV and 0.3 eV, respectively. Meanwhile, the binding energies of the characteristic peaks of C1s and N1s basically remained unchanged (Fig. S9 and S10[†]). Such observed shifts for both Zr 3d and Ti 2p implied the electron migration from TiO_2 and $\text{NH}_2\text{-UiO-66}$ to Au through an internal electric field formed at the interface of TiO_2 and $\text{NH}_2\text{-UiO-66}$, in well agreement with previous reports.^{51,52} These shifts might also be indicative of the formation of strong interfacial and charge interactions among the components in the 1 wt% Au- $\text{TiO}_2@NH_2\text{-UiO-66}$ nanocomposite. Moreover, as for $\text{TiO}_2@NH_2\text{-UiO-66}$ and 1 wt% Au- $\text{TiO}_2@NH_2\text{-UiO-66}$, the charge interactions among the components would be closely relevant to the decreases in their band gap energies compared to both pure TiO_2 and $\text{NH}_2\text{-UiO-66}$ (Fig. 3), and similar observations were also reported in the literature.^{53,54}

The charge transfer together with the separation capability of photogenerated electron-hole pairs is critical to the activities of photocatalysts; thus photoelectrochemical measurements including transient photocurrent responses and electrochemical impedance spectra (EIS), as well as photoluminescence (PL) emission spectra were obtained for the TiO_2 , $\text{NH}_2\text{-UiO-66}$, $\text{TiO}_2@NH_2\text{-UiO-66}$ and 1 wt% Au- $\text{TiO}_2@NH_2\text{-UiO-66}$ samples. Firstly, transient photocurrent responses *via* periodic on/off cycles were observed upon xenon lamp irradiation. As displayed in Fig. 6a, the photocurrents of the TiO_2 , $\text{NH}_2\text{-UiO-66}$, $\text{TiO}_2@NH_2\text{-UiO-66}$ and 1 wt% Au-

$\text{TiO}_2@NH_2\text{-UiO-66}$ samples all reached a maximum value promptly without any delay after switching on the light and then dropped to near zero quickly upon switching off the light. Moreover, no apparent decline in photocurrent density was observed during five successive cycles. These results demonstrated the fast dynamics of excitation and transfer of the photoelectrode as well as excellent reproducibility of the tests. For the pure TiO_2 and $\text{NH}_2\text{-UiO-66}$, they showed low photocurrent densities after turning on the light. Compared with pure TiO_2 and $\text{NH}_2\text{-UiO-66}$, the photocurrent density of the $\text{TiO}_2@NH_2\text{-UiO-66}$ sample was obviously increased, suggesting that the integration of TiO_2 into $\text{NH}_2\text{-UiO-66}$ could facilitate the separation of photogenerated electron-hole pairs. Strikingly, the 1 wt% Au- $\text{TiO}_2@NH_2\text{-UiO-66}$ nanocomposite exhibits the highest photocurrent density, indicating that the cooperation among Au, TiO_2 and $\text{NH}_2\text{-UiO-66}$ made Au- $\text{TiO}_2@NH_2\text{-UiO-66}$ possess the superior lifetime of photogenerated electron-hole pairs.

It is well accepted that a lower PL intensity generally means a faster separation ability of photogenerated carriers. Therefore, PL spectra were also measured to obtain the separation ability of photogenerated carriers over the $\text{NH}_2\text{-UiO-66}$, $\text{TiO}_2@NH_2\text{-UiO-66}$ and 1 wt% Au- $\text{TiO}_2@NH_2\text{-UiO-66}$ samples. As presented in Fig. 6b, the 1 wt% Au- $\text{TiO}_2@NH_2\text{-UiO-66}$ nanocomposite exhibited the lowest PL intensity at nearly 465 nm, indicating that the incorporation of Au and TiO_2 into $\text{NH}_2\text{-UiO-66}$ played a crucial role in suppressing the recombination rate of photogenerated carriers compared with pure $\text{NH}_2\text{-UiO-66}$. Moreover, the PL result was consistent with the photocurrent results, further confirming that 1 wt% Au- $\text{TiO}_2@NH_2\text{-UiO-66}$ possessed the highest separation ability of photogenerated carriers.

To obtain deep insight into the charge transfer dynamics, the time-resolved PL spectra of the $\text{NH}_2\text{-UiO-66}$, $\text{TiO}_2@NH_2\text{-UiO-66}$ and 1 wt% Au- $\text{TiO}_2@NH_2\text{-UiO-66}$ samples were further measured and the decay curves of these three samples fitted a 3-exponential function (Fig. 6c and Table S2[†]). The results showed that the average decay lifetime of $\text{NH}_2\text{-UiO-66}$ was 358 ps. After the introduction of TiO_2 into $\text{NH}_2\text{-UiO-66}$, the average decay lifetime significantly declined to 100.47 ps. Notably, an apparently decreased lifetime value of 1 wt% Au- $\text{TiO}_2@NH_2\text{-UiO-66}$ was further observed, revealing that Au- $\text{TiO}_2@NH_2\text{-UiO-66}$ could effectively suppress the photogenerated electron-hole recombination. To further verify the above results, EIS was employed and the corresponding results are summarized in Fig. 6d. It was easy to find that the resistance radius was in the order of Au- $\text{TiO}_2@NH_2\text{-UiO-66}$ < $\text{TiO}_2@NH_2\text{-UiO-66}$ < TiO_2 < $\text{NH}_2\text{-UiO-66}$. The equivalent electrical circuit and the fitted electrical parameters are shown in Fig. S11 and Table S3.[†] The charge transfer resistance of TiO_2 , $\text{NH}_2\text{-UiO-66}$, $\text{TiO}_2@NH_2\text{-UiO-66}$ and 1 wt% Au- $\text{TiO}_2@NH_2\text{-UiO-66}$ was 11.47, 15.21, 3.67 and 2.89 k Ω , respectively. The EIS results were obviously coincident with the order of their photocurrent responses and PL results. These results definitely demonstrated that the heterojunction between TiO_2 and the MOF can accelerate the

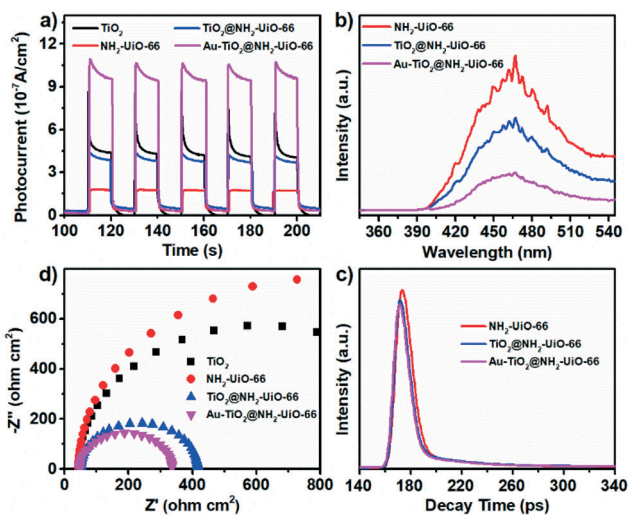


Fig. 6 Photocurrent responses (a), PL emission spectra (b), time-resolved PL spectra (c) and EIS Nyquist plots (d).

electron transport but the improvement was limited. The further introduction of Au could substantially boost the electron transfer due to its induced internal electric field and intrinsic conductivity, thus giving rise to excellent separation ability of photogenerated carriers. The significant differences in both the separation ability of photogenerated carriers and interfacial charge transfer among the TiO_2 , $\text{NH}_2\text{-UiO-66}$, $\text{TiO}_2@\text{NH}_2\text{-UiO-66}$ and 1 wt% $\text{Au-TiO}_2@\text{NH}_2\text{-UiO-66}$ samples should be responsible for their possible difference in photocatalytic activity.

Many noble metals, such as Au, Ag and Pt, have been proven to induce localized temperature increase by converting incident light under illumination due to their excellent LSPR, which plays a positive role in photocatalytic reactions.^{9,45,55,56} Therefore, an infrared radiation thermometer was also employed to monitor the time-dependent temperature curves of the TiO_2 , pure $\text{NH}_2\text{-UiO-66}$, $\text{TiO}_2@\text{NH}_2\text{-UiO-66}$ and 1 wt% $\text{Au-TiO}_2@\text{NH}_2\text{-UiO-66}$ samples under xenon lamp irradiation. When exposed to the irradiation of the xenon lamp, the surface temperature of all the above samples rapidly increased and then gradually tended to be stable (Fig. 7a). Nevertheless, the surface temperature increase of $\text{TiO}_2@\text{NH}_2\text{-UiO-66}$ was approximately 30.0 °C after 600 s of irradiation, whereas TiO_2 and pure $\text{NH}_2\text{-UiO-66}$ in control experiments boosted the surface temperature by 16.9 and 25.9 °C, respectively, suggesting that the incorporation of TiO_2 into $\text{NH}_2\text{-UiO-66}$ lacked the ability to effectively convert incident light into thermal energy. Interestingly, the temperature of 1 wt% $\text{Au-TiO}_2@\text{NH}_2\text{-UiO-66}$ promptly increased from 30.2 °C to 80.4 °C once exposed to light irradiation, which was obviously higher than that of $\text{TiO}_2@\text{NH}_2\text{-UiO-66}$. The outstanding temperature increase of

$\text{Au-TiO}_2@\text{NH}_2\text{-UiO-66}$ after irradiation could be associated with the excellent photothermal conversion capacity of Au induced by its LSPR.

To obtain the semiconductor characteristics, Mott-Schottky analyses at frequencies of 500 and 800 Hz were also performed. The slopes of the achieved C^{-2} versus the applied potential to the TiO_2 , pure $\text{NH}_2\text{-UiO-66}$, $\text{TiO}_2@\text{NH}_2\text{-UiO-66}$ and 1 wt% $\text{Au-TiO}_2@\text{NH}_2\text{-UiO-66}$ samples all presented positive values (Fig. 7b and S12–S14[†]), revealing that the samples were n-type semiconductors. According to the Mott-Schottky equation, the flat band potentials could be obtained by extrapolating the x-intercept. Because the CB edge potential of an n-type semiconductor is often more negative by approximately -0.1 V than the corresponding flat band potential,⁵⁷ the conduction bands of TiO_2 , pure $\text{NH}_2\text{-UiO-66}$, $\text{TiO}_2@\text{NH}_2\text{-UiO-66}$ and 1 wt% $\text{Au-TiO}_2@\text{NH}_2\text{-UiO-66}$ were estimated to be -0.61, -0.93, -0.92 and -0.90 V versus Ag/AgCl (*i.e.*, -0.31, -0.63, -0.62 and -0.60 V versus NHE), respectively. Obviously, the CB potential energy of TiO_2 was slightly more negative than the O_2/O_2^- standard potential, indicating that the photogenerated e^- on the surface of TiO_2 under light irradiation have the potential to reduce O_2 for the formation of $\cdot\text{O}_2^-$ radicals. Furthermore, the other three photocatalysts with more negative CB potential energies were likely to generate $\cdot\text{O}_2^-$ radicals more easily compared to TiO_2 . Based on the equation: $E_{\text{VB}} = E_{\text{CB}} + E_g$, the valence band (VB) potentials of TiO_2 , pure $\text{NH}_2\text{-UiO-66}$, $\text{TiO}_2@\text{NH}_2\text{-UiO-66}$ and 1 wt% $\text{Au-TiO}_2@\text{NH}_2\text{-UiO-66}$ were calculated to be 2.94, 2.28, 2.28 and 2.21 V vs. NHE, respectively. It is common knowledge that the standard redox potential of $\text{H}_2\text{O}/\cdot\text{OH}$ is approximately 2.37 V, which was apparently more negative than the VB potential of TiO_2 and more positive than the VB potentials of the other three photocatalysts (Fig. 7b and S12–S14[†]). Therefore, the photogenerated holes in the VB of TiO_2 have the potential to oxidize H_2O to form $\cdot\text{OH}$, while the other three photocatalysts have no ability to produce $\cdot\text{OH}$ by oxidizing H_2O with their photogenerated holes.

In order to further verify the formed active oxygen species on the surface of the photocatalyst, EPR tests were performed to analyse the potential active oxygen radicals including $\cdot\text{O}_2^-$ and $\cdot\text{OH}$. As expected, characteristic signals of $\text{DMPO}\cdot\text{O}_2^-$ were observed on all the samples (Fig. 7c), which could be associated with the more negative potential energy of their CB electrons (Fig. 7b and S12–S14[†]) than the O_2/O_2^- standard potential. Significantly, the signal intensity of $\text{DMPO}\cdot\text{O}_2^-$ on the samples followed the order of 1 wt% $\text{Au-TiO}_2@\text{NH}_2\text{-UiO-66}$ > $\text{TiO}_2@\text{NH}_2\text{-UiO-66}$ \approx $\text{NH}_2\text{-UiO-66}$ > TiO_2 . As indicated by the VB potentials of pure $\text{NH}_2\text{-UiO-66}$, $\text{TiO}_2@\text{NH}_2\text{-UiO-66}$ and 1 wt% $\text{Au-TiO}_2@\text{NH}_2\text{-UiO-66}$, they seemed incapable of generating $\cdot\text{OH}$ via the oxidation of H_2O by their photogenerated holes. However, a weak and unnoticeable $\text{DMPO}\cdot\text{OH}$ signal appeared on pure $\text{NH}_2\text{-UiO-66}$ (Fig. 7d), which should result from the primary $\cdot\text{O}_2^-$ on the CB along the path of $e^-/\text{O}_2 \rightarrow \cdot\text{O}_2^- \rightarrow \text{H}_2\text{O}_2 \rightarrow \cdot\text{OH}$ according to early references.^{58,59} Strikingly, the $\text{TiO}_2@\text{NH}_2\text{-UiO-66}$ nanocomposite exhibited a distinctly stronger

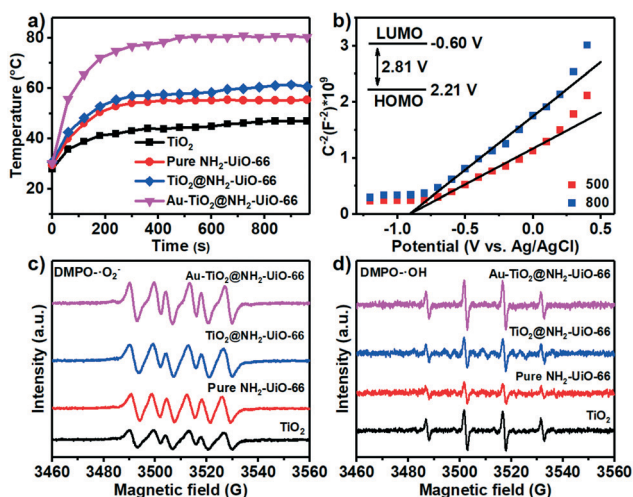


Fig. 7 Time-dependent temperature curves of TiO_2 , pure $\text{NH}_2\text{-UiO-66}$, $\text{TiO}_2@\text{NH}_2\text{-UiO-66}$ and 1 wt% $\text{Au-TiO}_2@\text{NH}_2\text{-UiO-66}$ under simulated solar light irradiation (a). Mott-Schottky plots for 1 wt% $\text{Au-TiO}_2@\text{NH}_2\text{-UiO-66}$ at frequencies of 500 and 800 Hz (b). DMPO spin-trapping EPR spectra recorded at ambient temperature in the presence of photocatalysts for $\text{DMPO}\cdot\text{O}_2^-$ formed in the irradiated methanol dispersion (c), and $\text{DMPO}\cdot\text{OH}$ formed in the irradiated H_2O dispersion (d).

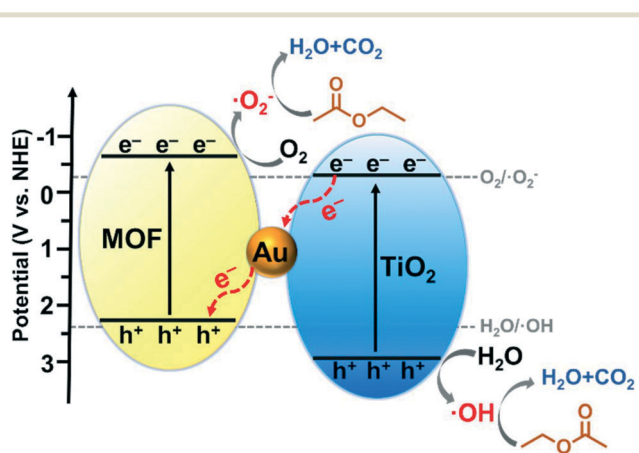
DMPO- $\cdot\text{OH}$ signal than pure $\text{NH}_2\text{-UiO-66}$ but a bit lower than pure TiO_2 . Given the signal intensities of both DMPO- $\cdot\text{O}_2^-$ and DMPO- $\cdot\text{OH}$ on TiO_2 , pure $\text{NH}_2\text{-UiO-66}$, and $\text{TiO}_2@\text{NH}_2\text{-UiO-66}$, it could be concluded that the photogenerated electrons in the CB of TiO_2 might transfer to the VB of $\text{NH}_2\text{-UiO-66}$, leaving photogenerated holes in TiO_2 and photogenerated electrons in $\text{NH}_2\text{-UiO-66}$ to oxidize ethyl acetate. Consequently, the Z-scheme heterojunction mechanism can well interpret the presence of DMPO- $\cdot\text{O}_2^-$ and DMPO- $\cdot\text{OH}$ signals. Importantly, the increased signal intensities of DMPO- $\cdot\text{O}_2^-$ and DMPO- $\cdot\text{OH}$ were further observed on 1 wt% Au- $\text{TiO}_2@\text{NH}_2\text{-UiO-66}$, which could be closely related to the introduction of tiny Au clusters as electron mediators to accelerate the transfer of photogenerated carriers. The remarkable enhancement in the signal intensities of DMPO- $\cdot\text{O}_2^-$ and DMPO- $\cdot\text{OH}$ of 1 wt% Au- $\text{TiO}_2@\text{NH}_2\text{-UiO-66}$ should be responsible for its optimum photocatalytic performance.

Based on the above results, we attempted to propose a plausible reaction mechanism for the photocatalytic degradation of ethyl acetate over Au- $\text{TiO}_2@\text{NH}_2\text{-UiO-66}$ as shown in Scheme 2. It is widely accepted that the plasmonic metal in a semiconductor photocatalyst could improve the separation efficiency of photogenerated electron-hole pairs *via* a local electromagnetic field enhancement induced by the internal electric field.⁴³ As demonstrated by the results of XPS, time-resolved PL and EIS Nyquist plots, the 1 wt% Au- $\text{TiO}_2@\text{NH}_2\text{-UiO-66}$ nanocomposite formed an internal electric field at the interface of TiO_2 and $\text{NH}_2\text{-UiO-66}$ aside from the strong interfacial interaction appearing in $\text{TiO}_2@\text{NH}_2\text{-UiO-66}$, which made Au- $\text{TiO}_2@\text{NH}_2\text{-UiO-66}$ exhibit faster charge transfer dynamics than $\text{TiO}_2@\text{NH}_2\text{-UiO-66}$. Under xenon light irradiation, the Au clusters with excellent LSPR would act as the UV-vis light photosensitizer to improve the light-harvesting ability of Au- $\text{TiO}_2@\text{NH}_2\text{-UiO-66}$, while TiO_2 and $\text{NH}_2\text{-UiO-66}$ worked as semiconductors to generate photogenerated carriers. Subsequently, the photogenerated

electrons on the CB of TiO_2 transfer quickly to the VB of $\text{NH}_2\text{-UiO-66}$ with the aid of the Au electron mediator and the formed internal electric field at the interface, and then recombine with the photogenerated holes on the VB of $\text{NH}_2\text{-UiO-66}$. As a consequence, the photogenerated electrons on the CB of $\text{NH}_2\text{-UiO-66}$ with a higher reduction potential and the holes on the VB of TiO_2 with a higher oxidation potential would be retained. This spatial separation of photogenerated electrons and holes would effectively prevent photogenerated charge recombination. Simultaneously, the retained photogenerated electrons and holes would reduce the adsorbed O_2 on the photocatalyst surface to produce $\cdot\text{O}_2^-$ radicals and react with the adsorbed H_2O to produce highly reactive $\cdot\text{OH}$ radicals, respectively. Additionally, the configuration of $\text{NH}_2\text{-UiO-66}$ encapsulated TiO_2 and Au made ethyl acetate and the intermediates highly accessible to the active species because the adsorbed substrate and photocatalytically active sites are located in the same interconnected 3D open space in MOFs. Therefore, the formed $\cdot\text{O}_2^-$, $\cdot\text{OH}$ and holes as dominating active species would readily attack and degrade ethyl acetate due to the high contact probability between the active species and substrates. On the other hand, as observed using the infrared radiation thermometer (Fig. 7a), 1 wt% Au- $\text{TiO}_2@\text{NH}_2\text{-UiO-66}$ enhanced the surface temperature by 50.2 °C after 600 s of irradiation which originated from the LSPR of Au, whereas the surface temperature of TiO_2 , pure $\text{NH}_2\text{-UiO-66}$ and $\text{TiO}_2@\text{NH}_2\text{-UiO-66}$ used as control experiments only raised by 16.9, 25.9 and 30.0 °C, respectively. This photothermal effect induced by the non-radiative decay process of LSPR could be used for the thermal activation of substrates to promote the photocatalytic reaction.⁶⁰ Finally, the cooperative effect between the charge space separated Z-scheme heterostructure and the LSPR of Au enabled Au- $\text{TiO}_2@\text{NH}_2\text{-UiO-66}$ to smoothly degrade ethyl acetate to CO_2 and H_2O under xenon light irradiation. Considered that the light absorption, photothermal effect and electron transfer of the photocatalyst are readily adjustable *via* simply changing the morphology of Au and constructing a semiconductor heterostructure, it would offer the opportunity to design more effective photocatalysts for VOC degradation in future endeavors. Thus, Au- $\text{TiO}_2@\text{NH}_2\text{-UiO-66}$ can't exhibit the highest photocatalytic activity relative to previous reports (Table S4[†]), but the concept for the construction of photocatalysts holds great promise for enhanced activity.

Conclusions

In summary, a charge space separated Z-scheme heterostructure photocatalyst was successfully constructed by the encapsulation of tiny TiO_2 and Au into $\text{NH}_2\text{-UiO-66}$ with Au nanoclusters as electron mediators. High porous $\text{NH}_2\text{-UiO-66}$ with interconnected 3D pores encapsulating Au and TiO_2 was not only beneficial to the fast diffusion of substrates, but also shortened the transport distance between the substrates and the reactive substrates, thus improving



Scheme 2 Possible reaction mechanism for the photocatalytic oxidation of ethyl acetate over Au- $\text{TiO}_2@\text{NH}_2\text{-UiO-66}$ under visible light irradiation.

the opportunities for the oxidation of typical VOCs, such as ethyl acetate. More importantly, the synergy between the formed internal electric field induced by Au and the charge space separated Z-scheme structure made the photogenerated carriers separate effectively. Remarkably, this significant enhancement in photogenerated electron-hole separation has been systematically evidenced by photoelectrochemical measurements, steady-state PL spectra and time-resolved PL spectra. As a result, Au-TiO₂@NH₂-UiO-66 would generate abundant strong oxidative species, including photogenerated holes, ·O₂⁻ and ·OH radicals, to attack ethyl acetate. Meanwhile, the heat induced by the LSPR of Au would also facilitate the photocatalytic oxidation of ethyl acetate. Finally, the obtained Au-TiO₂@NH₂-UiO-66 can greatly raise the photocatalytic activity compared with its corresponding semiconductors, including TiO₂, NH₂-UiO-66, Au/TiO₂, Au/NH₂-UiO-66 and TiO₂@NH₂-UiO-66. In particular, 1 wt% Au-TiO₂@NH₂-UiO-66 exhibits an exceptionally high mineralization efficiency of 85% with a degradation efficiency of 94.6% for ethyl acetate. This work might offer a particular perspective on the construction of superior photocatalysts based on MOFs and even other porous semiconductors for the visible-light-driven photocatalytic degradation of air pollutants.

Conflicts of interest

There are no conflicts to declare.

Acknowledgements

This work was supported by the National Natural Science Foundation of China (41991314, 41731279 and 22076028), Guangdong Provincial Key R&D Program (2019B110206002), Local Innovative and Research Teams Project of Guangdong Pearl River Talents Program (2017BT01Z032), Pearl River S&T Nova Program of Guangzhou (201806010177), and Natural Science Foundation of Guangdong (2019A1515010989).

Notes and references

- Q. Li and F. T. Li, Recent advances in surface and interface design of photocatalysts for the degradation of volatile organic compounds, *Adv. Colloid Interface Sci.*, 2020, **284**, 102275.
- Y. Ji, Q. Shi, Y. Li, T. An, J. Zheng, J. Peng, Y. Gao, J. Chen, G. Li, Y. Wang, F. Zhang, A. L. Zhang, J. Zhao, M. J. Molina and R. Zhang, Carbenium ion-mediated oligomerization of methylglyoxal for secondary organic aerosol formation, *Proc. Natl. Acad. Sci. U. S. A.*, 2020, **117**, 13294–13299.
- C. He, J. Cheng, X. Zhang, M. Douthwaite, S. Patisson and Z. Hao, Recent Advances in the Catalytic Oxidation of Volatile Organic Compounds: A Review Based on Pollutant Sorts and Sources, *Chem. Rev.*, 2019, **119**, 4471–4568.
- C. T. Yang, G. Miao, Y. H. Pi, Q. B. Xia, J. L. Wu, Z. Li and J. Xiao, Abatement of various types of VOCs by adsorption/catalytic oxidation: A review, *Chem. Eng. J.*, 2019, **370**, 1128–1153.
- J. Ji, X. L. Lu, C. Chen, M. He and H. B. Huang, Potassium-modulated delta-MnO₂ as robust catalysts for formaldehyde oxidation at room temperature, *Appl. Catal., B*, 2020, **260**, 118210.
- H. Liu, M. Xu, G. Li, W. Zhang and T. An, Solar-light-triggered regenerative adsorption removal of styrene by silver nanoparticles incorporated in metal-organic frameworks, *Environ. Sci.: Nano*, 2021, **8**, 543–553.
- X. Zhang, B. Gao, A. E. Creamer, C. Cao and Y. Li, Adsorption of VOCs onto engineered carbon materials: A review, *J. Hazard. Mater.*, 2017, **338**, 102–123.
- Y. Boyjoo, H. Sun, J. Liu, V. K. Pareek and S. Wang, A review on photocatalysis for air treatment: From catalyst development to reactor design, *Chem. Eng. J.*, 2017, **310**, 537–559.
- W. Ji, Z. Rui and H. Ji, Z-scheme Ag₃PO₄/Ag/SrTiO₃ Heterojunction for Visible-Light Induced Photothermal Synergistic VOCs Degradation with Enhanced Performance, *Ind. Eng. Chem. Res.*, 2019, **58**, 13950–13959.
- H. L. Liu, Y. P. Ma, J. Y. Chen, M. C. Wen, G. Y. Li and T. C. An, Highly efficient visible-light-driven photocatalytic degradation of VOCs by CO₂-assisted synthesized mesoporous carbon confined mixed-phase TiO₂ nanocomposites derived from MOFs, *Appl. Catal., B*, 2019, **250**, 337–346.
- F. He, U. Muliane, S. Weon and W. Choi, Substrate-specific mineralization and deactivation behaviors of TiO₂ as an air-cleaning photocatalyst, *Appl. Catal., B*, 2020, **275**, 119145.
- P. Yao, H. Liu, D. Wang, J. Chen, G. Li and T. An, Enhanced visible-light photocatalytic activity to volatile organic compounds degradation and deactivation resistance mechanism of titania confined inside a metal-organic framework, *J. Colloid Interface Sci.*, 2018, **522**, 174–182.
- W. Cui, J. Y. Li, L. C. Chen, X. A. Dong, H. Wang, J. P. Sheng, Y. J. Sun, Y. Zhou and F. Dong, Nature-inspired CaCO₃ loading TiO₂ composites for efficient and durable photocatalytic mineralization of gaseous toluene, *Sci. Bull.*, 2020, **65**, 1626–1634.
- Z. Shayegan, C. S. Lee and F. Haghghat, TiO₂ photocatalyst for removal of volatile organic compounds in gas phase-A review, *Chem. Eng. J.*, 2018, **334**, 2408–2439.
- H. Chen, C. E. Nanayakkara and V. H. Grassian, Titanium dioxide photocatalysis in atmospheric chemistry, *Chem. Rev.*, 2012, **112**, 5919–5948.
- W. P. Zhang, G. Y. Li, H. L. Liu, J. Y. Chen, S. T. Ma, M. C. Wen, J. J. Kong and T. C. An, Photocatalytic degradation mechanism of gaseous styrene over Au/TiO₂@CNTs: Relevance of superficial state with deactivation mechanism, *Appl. Catal., B*, 2020, **272**, 118969.
- W. Zhang, G. Li, H. Liu, J. Chen, S. Ma and T. An, Micro/nano-bubble assisted synthesis of Au/TiO₂@CNTs composite photocatalyst for photocatalytic degradation of gaseous styrene and its enhanced catalytic mechanism, *Environ. Sci.: Nano*, 2019, **6**, 948–958.

- 18 J. Shi, J. Chen, G. Li, T. An and H. Yamashita, Fabrication of Au/TiO₂ nanowires@carbon fiber paper ternary composite for visible-light photocatalytic degradation of gaseous styrene, *Catal. Today*, 2017, **281**, 621–629.
- 19 Q. Xu, L. Zhang, J. Yu, S. Wageh, A. A. Al-Ghamdi and M. Jaroniec, Direct Z-scheme photocatalysts: Principles, synthesis, and applications, *Mater. Today*, 2018, **21**, 1042–1063.
- 20 J. X. Low, C. Jiang, B. Cheng, S. Wageh, A. A. Al-Ghamdi and J. G. Yu, A Review of Direct Z-Scheme Photocatalysts, *Small Methods*, 2017, **1**, 1700080.
- 21 Y. You, S. Wang, K. Xiao, T. Ma, Y. Zhang and H. Huang, Z-Scheme g-C₃N₄/Bi₄NbO₈Cl Heterojunction for Enhanced Photocatalytic Hydrogen Production, *ACS Sustainable Chem. Eng.*, 2018, **6**, 16219–16227.
- 22 J. X. Low, B. Z. Dai, T. Tong, C. J. Jiang and J. G. Yu, In Situ Irradiated X-Ray Photoelectron Spectroscopy Investigation on a Direct Z-Scheme TiO₂/CdS Composite Film Photocatalyst, *Adv. Mater.*, 2019, **31**, 1802981.
- 23 X. L. Liu, Q. Z. Zhang and D. L. Ma, Advances in 2D/2D Z-scheme heterojunctions for photocatalytic applications, *Sol. RRL*, 2021, **5**, 2000397.
- 24 W. H. Zhang, A. R. Mohamed and W. J. Ong, Z-Scheme Photocatalytic Systems for Carbon Dioxide Reduction: Where Are We Now?, *Angew. Chem., Int. Ed.*, 2020, **59**, 22894–22915.
- 25 X. Li, C. Garlisi, Q. Guan, S. Anwer, K. Al-Ali, G. Palmisano and L. Zheng, A review of material aspects in developing direct Z-scheme photocatalysts, *Mater. Today*, 2021, DOI: 10.1016/j.mattod.2021.02.017.
- 26 J. D. Xiao, Q. Shang, Y. Xiong, Q. Zhang, Y. Luo, S. H. Yu and H. L. Jiang, Boosting photocatalytic hydrogen production of a metal-organic framework decorated with platinum nanoparticles: the platinum location matters, *Angew. Chem., Int. Ed.*, 2016, **55**, 9389–9393.
- 27 X. N. Ren, Z. Y. Hu, J. Jin, L. Wu, C. Wang, J. Liu, F. Liu, M. Wu, Y. Li, G. V. Tendeloo and B. L. Su, Cocatalyzing Pt/PtO phase-junction nanodots on hierarchically porous TiO₂ for highly enhanced photocatalytic hydrogen production, *ACS Appl. Mater. Interfaces*, 2017, **9**, 29687–29698.
- 28 T. Xu, S. Wang, L. Li and X. Liu, Dual templated synthesis of tri-modal porous SrTiO₃/TiO₂@carbon composites with enhanced photocatalytic activity, *Appl. Catal., A*, 2019, **575**, 132–141.
- 29 M. Wen, G. Li, H. Liu, J. Chen, T. An and H. Yamashita, Metal-organic framework-based nanomaterials for adsorption and photocatalytic degradation of gaseous pollutants: recent progress and challenges, *Environ. Sci.: Nano*, 2019, **6**, 1006–1025.
- 30 X. Zhang, Z. Chen, X. Liu, S. L. Hanna, X. Wang, R. Taheri-Ledari, A. Maleki, P. Li and O. K. Farha, A historical overview of the activation and porosity of metal-organic frameworks, *Chem. Soc. Rev.*, 2020, **49**, 7406–7427.
- 31 R. Q. Fang, A. Dhakshinamoorthy, Y. W. Li and H. Garcia, Metal organic frameworks for biomass conversion, *Chem. Soc. Rev.*, 2020, **49**, 3638–3687.
- 32 P. X. Li, X. Y. Yan, X. M. Song, J. J. Li, B. H. Ren, S. Y. Gao and R. Cao, Zirconium-Based metal-organic framework particle films for visible-light-driven efficient photoreduction of CO₂, *ACS Sustainable Chem. Eng.*, 2021, **9**, 2319–2325.
- 33 L. Chi, Q. Xu, X. Y. Liang, J. D. Wang and X. T. Su, Iron-Based Metal-Organic Frameworks as Catalysts for Visible Light-Driven Water Oxidation, *Small*, 2016, **12**, 1351–1358.
- 34 Y. Fu, D. Sun, Y. Chen, R. Huang, Z. Ding, X. Fu and Z. Li, An Amine-Functionalized Titanium Metal-Organic Framework Photocatalyst with Visible-Light-Induced Activity for CO₂ Reduction, *Angew. Chem., Int. Ed.*, 2012, **51**, 3364–3367.
- 35 C. Gomes Silva, I. Luz, F. X. Llabrés i Xamena, A. Corma and H. García, Water Stable Zr-Benzenedicarboxylate Metal-Organic Frameworks as Photocatalysts for Hydrogen Generation, *Chem. – Eur. J.*, 2010, **16**, 11133–11138.
- 36 X. Ding, H. Liu, J. Chen, M. Wen, G. Li, T. An and H. Zhao, In situ growth of well-aligned Ni-MOF nanosheets on nickel foam for enhanced photocatalytic degradation of typical volatile organic compounds, *Nanoscale*, 2020, **12**, 9462–9470.
- 37 T. Zeng, D. Shi, Q. Cheng, G. Liao, H. Zhou and Z. Pan, Construction of novel phosphonate-based MOF/P-TiO₂ heterojunction photocatalysts: enhanced photocatalytic performance and mechanistic insight, *Environ. Sci.: Nano*, 2020, **7**, 861–879.
- 38 Q. Huo, X. Qi, J. Li, G. Liu, Y. Ning, X. Zhang, B. Zhang, Y. Fu and S. Liu, Preparation of a direct Z-scheme α-Fe₂O₃/MIL-101(Cr) hybrid for degradation of carbamazepine under visible light irradiation, *Appl. Catal., B*, 2019, **255**, 117751.
- 39 L. Wang, P. Jin, J. Huang, H. She and Q. Wang, Integration of copper(II)-porphyrin zirconium metal-organic framework and titanium dioxide to construct Z-scheme system for highly improved photocatalytic CO₂ reduction, *ACS Sustainable Chem. Eng.*, 2019, **7**, 15660–15670.
- 40 F. Mu, Q. Cai, H. Hu, J. Wang, Y. Wang, S. Zhou and Y. Kong, Construction of 3D UiO-66-(COOH)₂/ZnIn₂S₄ hybrid decorated with non-noble MoS₂ cocatalyst: A highly efficient photocatalyst for hydrogen evolution and Cr(VI) reduction, *Chem. Eng. J.*, 2020, **384**, 123352.
- 41 S. Subudhi, S. Mansingh, G. Swain, A. Behera, D. Rath and K. Parida, HPW-anchored UiO-66 metal-organic framework: a promising photocatalyst effective toward tetracycline hydrochloride degradation and H₂ evolution via Z-scheme charge dynamics, *Inorg. Chem.*, 2019, **58**, 4921–4934.
- 42 S. Subudhi, S. P. Tripathy and K. Parida, Metal oxide integrated metal organic frameworks (MO@MOF): rational design, fabrication strategy, characterization and emerging photocatalytic applications, *Inorg. Chem. Front.*, 2021, **8**, 1619–1636.
- 43 S. X. Zhong, Y. M. Xi, Q. Chen, J. R. Chen and S. Bai, Bridge engineering in photocatalysis and photoelectrocatalysis, *Nanoscale*, 2020, **12**, 5764–5791.
- 44 S. Subudhi, S. Mansingh, S. P. Tripathy, A. Mohanty, P. Mohapatra, D. Rath and K. Parida, The fabrication of Au/Pd plasmonic alloys on UiO-66-NH₂: an efficient visible light-induced photocatalyst towards the Suzuki Miyaura coupling reaction under ambient conditions, *Catal. Sci. Technol.*, 2019, **9**, 6585–6597.

- 45 T. A. Tabish, P. Dey, S. Mosca, M. Salimi, F. Palombo, P. Matousek and N. Stone, Smart Gold Nanostructures for Light Mediated Cancer Theranostics: Combining Optical Diagnostics with Photothermal Therapy, *Adv. Sci.*, 2020, 7, 1903441.
- 46 F. Vermoortele, R. Ameloot, A. Vimont, C. Serre and D. De Vos, An amino-modified Zr-terephthalate metal-organic framework as an acid-base catalyst for cross-aldol condensation, *Chem. Commun.*, 2011, 47, 1521–1523.
- 47 T. Bein, Ultrasmall Titania Nanocrystals and Their Direct Assembly into Mesoporous Structures Showing Fast Lithium Insertion, *J. Am. Chem. Soc.*, 2010, 132, 12605–12611.
- 48 S. Subudhi, L. Paramanik, S. Sultana, S. Mansingh, P. Mohapatra and K. Parida, A type-II interband alignment heterojunction architecture of cobalt titanate integrated UiO-66-NH₂: A visible light mediated photocatalytic approach directed towards Norfloxacin degradation and green energy (Hydrogen) evolution, *J. Colloid Interface Sci.*, 2020, 568, 89–105.
- 49 Y. Gu, H. Yang, B. Li, J. Mao and Y. An, A ternary nanooxide NiO-TiO₂-ZrO₂/SO₄²⁻ as efficient solid superacid catalysts for electro-oxidation of glucose, *Electrochim. Acta*, 2016, 194, 367–376.
- 50 Q. Yang, W. X. Liu, B. Q. Wang, W. N. Zhang, X. Q. Zeng, C. Zhang, Y. J. Qin, X. M. Sun, T. P. Wu, J. F. Liu, F. W. Huo and J. Lu, Regulating the spatial distribution of metal nanoparticles within metal-organic frameworks to enhance catalytic efficiency, *Nat. Commun.*, 2017, 8, 14429.
- 51 Y. Liu, X. Zeng, C. D. Easton, Q. Li, Y. Xia, Y. Yin, X. Hu, J. Hu, D. Xia, D. T. McCarthy, A. Deletic, C. Sun, J. Yu and X. Zhang, An in situ assembled WO₃-TiO₂ vertical heterojunction for enhanced Z-scheme photocatalytic activity, *Nanoscale*, 2020, 12, 8775–8784.
- 52 J. Wang, S. J. Sun, H. Ding, W. Li and X. Wang, Well-Designed CdS/TiO₂/MS-SiO₂ Z-Scheme Photocatalyst for Combating Poison with Poison, *Ind. Eng. Chem. Res.*, 2020, 59, 7659–7669.
- 53 D. Gogoi, A. Namdeo, A. K. Golder and N. R. Peela, Ag-doped TiO₂ photocatalysts with effective charge transfer for highly efficient hydrogen production through water splitting, *Int. J. Hydrogen Energy*, 2020, 45, 2729–2744.
- 54 L. Collado, A. Reynal, F. Fresno, M. Barawi, C. Escudero, V. Perez-Dieste, J. M. Coronado, D. P. Serrano, J. R. Durrant and V. A. de la Pena O'Shea, Unravelling the effect of charge dynamics at the plasmonic metal/semiconductor interface for CO₂ photoreduction, *Nat. Commun.*, 2018, 9, 4986.
- 55 C. Kuppe, K. R. Rusimova, L. Ohnoutek, D. Slavov and V. K. Valev, "Hot" in Plasmonics: Temperature-Related Concepts and Applications of Metal Nanostructures, *Adv. Opt. Mater.*, 2020, 8, 1901166.
- 56 F. Wang, Q. Li and D. Xu, Recent Progress in Semiconductor-Based Nanocomposite Photocatalysts for Solar-to-Chemical Energy Conversion, *Adv. Energy Mater.*, 2017, 7, 1700529.
- 57 F. He, B. C. Zhu, B. Cheng, J. G. Yu, W. K. Ho and W. Macyk, 2D/2D/0D TiO₂/C₃N₄/Ti₃C₂ MXene composite S-scheme photocatalyst with enhanced CO₂ reduction activity, *Appl. Catal., B*, 2020, 272, 119006.
- 58 M. Teranishi, S. Naya and H. Tada, In Situ Liquid Phase Synthesis of Hydrogen Peroxide from Molecular Oxygen Using Gold Nanoparticle-Loaded Titanium(IV) Dioxide Photocatalyst, *J. Am. Chem. Soc.*, 2010, 132, 7850–7851.
- 59 H. Sheng, H. Ji, W. Ma, C. Chen and J. Zhao, Direct Four-Electron Reduction of O₂ to H₂O on TiO₂ Surfaces by Pendant Proton Relay, *Angew. Chem., Int. Ed.*, 2013, 52, 9686–9690.
- 60 L. Yuan, Z. Geng, J. Xu, F. Guo and C. Han, Metal-semiconductor heterostructures for photoredox catalysis: where are we now and where do we go?, *Adv. Funct. Mater.*, 2021, 2101103, DOI: 10.1002/adfm.202101103.